Sucrose refractive index sensing characterization of laser processed optical fiber Fabry-Perot micro-cavity

QING TAO[1,2], YEGANG YIN[1], WENXIANG KUANG[1], LIANGPENG WEI[1], JIAN CHENG[1], BOWEN LU[3], DUN LIU[1,*]
[1]*Laser Group, School of Mechanical Engineering, Hubei University of Technology, Wuhan 430068, China*
[2]*Hubei Key Laboratory of Modern Manufacturing Quantity Engineering, School of Mechanical Engineering, Hubei University of Technology, Wuhan 430068, Hubei, P. R. China*
[3]*State Key Laboratory of Optical Fiber and Cable Manufacture Technology (YOFC), Wuhan 430068, China*

In this paper, a Fabry-Perot micro-cavity sensor have been successfully fabricated by femtosecond laser. The optimal etching parameters of Fabry-Perot micro-cavity are obtained. Length of Fabry-Perot micro-cavity is between 45 μm and 60 μm, height of Fabry-Perot micro-cavity is between 70 μm and 75 μm, and inclined angle of φ is less than 1.3°. The sensor exhibits better sucrose refractive index sensitivity of -30.69 dB/RIU and linearity of 98.7%. After using CL3-AMW method and improved data fusion algorithm, the sensitivity of sucrose refractive index attains -31.98 dB/RIU and linearity increases to 99.58%. The sensing performance of optical fiber Fabry-Perot micro-cavity is effective.

1. Introduction

With the rapid development of optical fiber sensing technology, the research of fiber sensors has received great attention [1-3]. There are three types of fiber sensors: optical fiber grating sensors [4-5], optical fiber surface plasmon resonance sensors [6-7], and optical fiber interference sensors [8-9]. As a typical optical interference structure, the optical fiber Fabry-Perot sensor is an optical device with extensive applications, which has remarkable stability, immunity to electromagnetic interference, and suitability for extreme environments [10]. Some physical quantities are measured, such as, pressure [11], strain [12], temperature [13], acceleration [14], and refractive index [15], and so on.

There are some fabrication methods about optical fiber Fabry-Perot sensors. A quartz capillary [16-17] is used to prepare non-intrinsic fiber Fabry-Perot sensors, but its end face is easily damaged by extending fiber into the capillary, which reduces the reflectivity. Arc discharge fusion techniques are reported, which include single-mode fiber to single-mode fiber fusion [18-19] and single-mode fiber to specialty fiber fusion. Its operational requirements are very difficult. Chemical etching is used to manufacture Fabry-Perot cavities in the fiber end face [20], chemical solution is prone to environmental pollution [21]. Femtosecond laser

processing offers several advantages, such as, the ability to control micro-cavity sizes and low thermal effect. Moreover, the heat-affected zone is minimized and mechanical damage is seldom, those ensure the precision [22-23].

For optical fiber Fabry-Perot sensing system, a reasonable and effective data analysis method plays an important role in the measuring accuracy. There are some signal processing methods, for example, single peak tracking method, peak-to-peak distance method, Fourier transformation method, and so on. Y. Li proposed a differential spectrum integration (SDI) method, which was validated in an optical fiber MZI refractive index sensor [24]. Di Wu used the SDI method in an optical fiber FPI refractive index sensor, and the sensitivity of refractive index was improved compared with the original analysis method [25]. However, its linearity and sensitivity still may be improved.

In this paper, an optical fiber Fabry-Perot microcavity is simulated and optimized, then, it is fabricated by femtosecond laser. The improved CL3 adaptive multiwavelet (CL3-AMW) method is employed to obtain the best reference interference spectrum. Then, the modified spectral differentiation integration (SDI) method has been utilized for demodulating the spectral information. In order to remove the gross error, an improved data fusion algorithm is proposed. The

experimental results demonstrate that optical fiber Fabry-Perot sensor has a good response to sucrose refractive index variations. The measuring sensitivity is -30.69 dB/RIU and linearity is 98.7% by original method. After using CL3-AMW method and improved data fusion algorithm, the refractive index sensitivity reaches -31.98 dB/RIU, linearity achieves 99.58%. Linearity and sensitivity are significantly better than the former. The proposed optimization algorithms have some significance for the development of optical fiber Fabry-Perot cavity refractive index sensors.

2. Theoretical analysis

2.1. Sensing theory of optical fiber F-P micro-cavity

The structure of optical fiber Fabry-Perot micro-cavity is shown in Fig. 1. The input light enters the optical fiber, first Fresnel reflection happens at the end-face M1, reflected light I_1 appears. The rest light passes through the micro-cavity to the end-face M2, reflected light I_2 occurs. I_1 and I_2 interfere with each other, interference spectrum generates. φ_1 is left end-face inclination, φ_2 is right end-face inclination. L is the length of micro-cavity, and H is the depth of micro-cavity. The optical fiber is a low-loss single-mode optical fiber produced by YOFC, with a core diameter of 9.8~10.8 μm and cladding diameter of 125±0.7 μm.
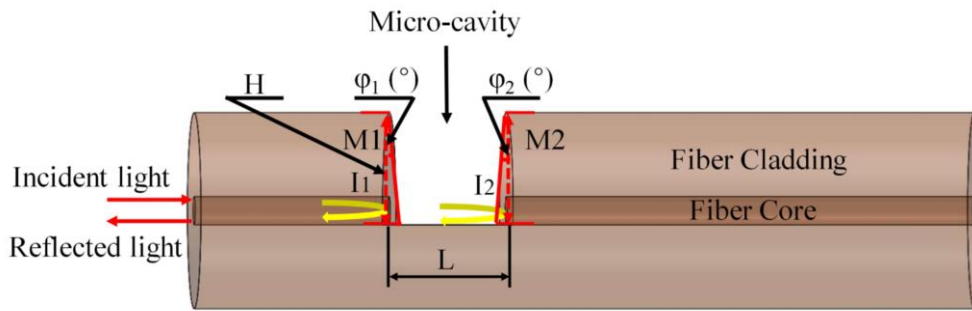

Fig. 1. Structure of optical fiber Fabry-Perot micro-cavity (color online)

The output light intensity of asymmetric optical fiber Fabry-Perot micro-cavity is [26],

$$I_R = \frac{a^2(r_1^2 + r_2^2 - 2r_1r_2\cos\varphi)}{1+(r_1r_2)^2 - 2r_1r_2\cos\varphi} \qquad (1)$$

$$I_T = \frac{a^2(1-r_1^2)}{1+(r_1r_2) - 2\cos\varphi} \qquad (2)$$

I_R and I_T are the output light intensity of reflection and transmission, respectively. r_1 and r_2 are the reflection coefficients of two reflectors in optical fiber Fabry-Perot micro-cavity. a is the amplitude of incident light. φ is the phase difference between two adjacent beams. The light intensity of reflected or transmitted light is a function of phase difference φ. The relationship between the phase difference φ and its optical path difference Δ and length L is [27],

$$\varphi = \frac{2\pi}{\lambda}\Delta \qquad (3)$$

$$\Delta = 2nL\cos\alpha \qquad (4)$$

λ is the wavelength and n is refractive index of medium in the micro-cavity. α is the angle between the incident light and the normal line of reflection plane among the two reflection surfaces. Then,

$$\varphi = \frac{4\pi}{\lambda}nL\cos\alpha \qquad (5)$$

The reflected light intensity is a function of cavity length L and wavelength λ in the formula (1) and (2). The phase difference between two reflected lights is proportional to the length L in the formula (5). When the length L changes, the phase difference φ also changes. The intensity of reflected light also changes.

For symmetric low reflectivity fiber Fabry-Perot micro-cavity,

$$r_1, r_2 << 1, r_1 = r_2 = r \tag{6}$$

The intensity of reflected light can be approximately expressed as,

$$I_R = 2a^2 r^2 (1 - \cos\varphi) = 2I_0 R(1 - \cos\varphi) \tag{7}$$

$I_0 = a^2$ is intensity of incident light and $R = r^2$ is reflectivity. The input light intensity I_0 is constant, the length L is a function of wavelength λ and reflected light intensity I_R. So, the measurand can be obtained by testing the reflected light intensity.

2.2. Optimal parameters for optical fiber micro-cavity

The relationship between the micro-cavity depth and normalized reflected interference light power (NRILP) is shown in Fig. 2. When the etching depth is less than 60 μm, the NRILP is basically stable, it is only 0.015, and the core of optical fiber is not damaged. While the etching depth is within 60 μm to 70 μm, the NRILP increases linearly, and the slope is 0.0078/μm, which partially destroys the core. When the etching depth is greater than 70 μm, the NRILP is still stable, it is 0.092, and the core is completely cut off. Higher NRILP can be obtained only when the etching depth is greater than 70 μm. However, it is important to note that the optical fiber is easier to break when the micro-cavity depth exceeds 80 μm. Therefore, optimal etching depth should be within 70 μm to 75 μm.
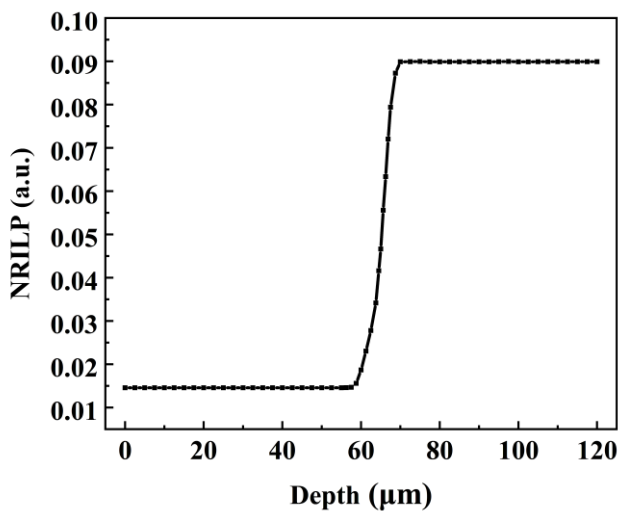

Fig. 2. Relationship between micro-cavity depth and NRILP

The influence of micro-cavity length on the NRILP is calculated in Fig. 3. The NRILP is more than 0.09, when L ∈ (45 μm, 60 μm). Similarly, the NRILP achieves

the maximum of 0.09434, when L=50 μm. The NRILP decreases faster, when L<45 μm or L>60 μm. Therefore, the NRILP is higher when L∈ (45 μm, 60 μm).
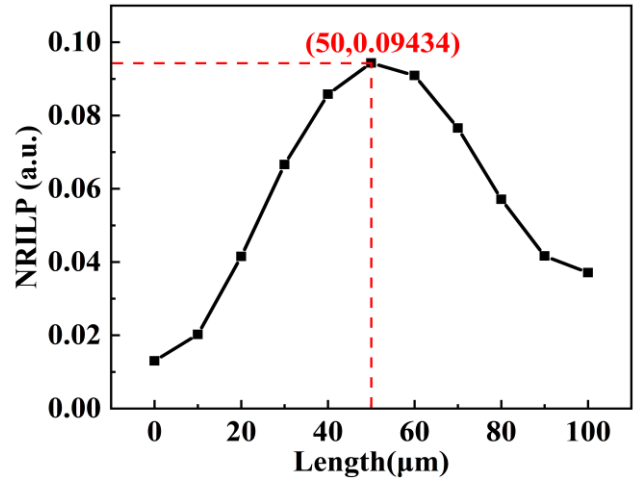

Fig. 3. Relationship between micro-cavity length and NRILP

When length and depth change simultaneously, the variation of NRILP is obtained in Fig. 4. The NRILP is more than 0.1, when L ∈ (45 μm, 60 μm) and H ∈ (70 μm, 75 μm).
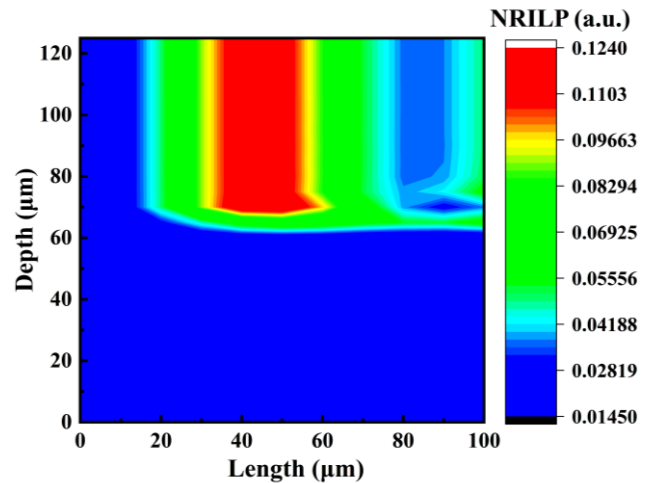

Fig. 4. Relationship between micro-cavity length & depth and NRILP (color online)

The longitudinal section of micro-cavity is an inverted trapezoid. The effect of end-face inclination ($\varphi = \varphi_1 = \varphi_2$) on the NRILP is obtained, and the simulation result is shown in Fig. 5. With the increase of end-face inclination [28], the NRILP first increases and then decreases, and finally tends to a stable value. When the inclination is 0.86°, NRILP reaches maximum of 0.112. The end-face inclination should be less than 1.3°, then, the NRILP is greater than 0.1.
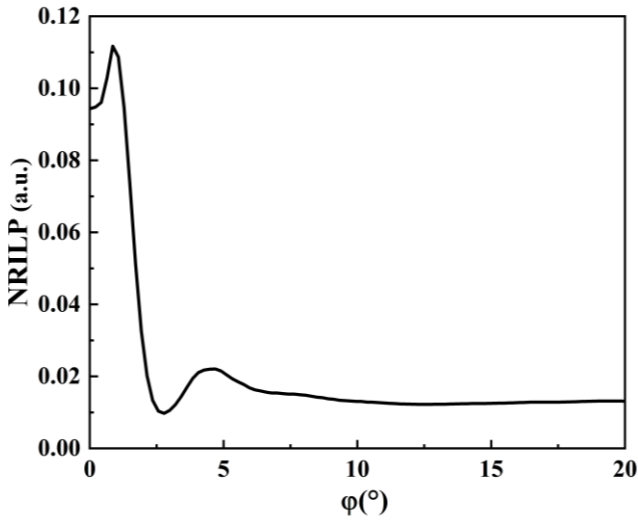
Fig. 5. Relationship between the end-face inclination and NRILP

So, the optimal parameters of micro-cavity are as follows: $L \in (45\ \mu m,\ 60\ \mu m)$, $H \in (70\ \mu m,\ 75\ \mu m)$, and φ is less than $1.3°$.

2.3. Theory of demodulation

For optical fiber Fabry-Perot sensors, the interference spectrum is demodulated with the changes of external refractive index, the contrast of interference stripe is calculated. The maximum stripe contrast (V) can be expressed as [29],

$$V = 10\log_{10}\left[\frac{I_{max}(\lambda)}{I_{min}(\lambda)}\right] \qquad (8)$$

I_{max} and I_{min} are the maximum and minimum light intensity, respectively. The stripe contrast of interference spectrum measured by different refractive index solutions will be different. The normalize maximum interference stripe contrast is calculated as follows [30]:

$$\eta = \frac{V - V_{min}}{V_{max} - V_{min}} \times 100\% \qquad (9)$$

The normalized reflection sensitivity (dI/dRI) of optical fiber Fabry-Perot micro-cavity is expressed by formula (10),

$$\frac{dI}{dRI} = [((1-\alpha_1)^2(1-R_1)^2 + (1-\alpha_1)\ (1-R_1)\ \cos(2\phi)/\sqrt{R_1 R_2})]\frac{dR_2}{dRI} \qquad (10)$$

α_1 and α_2 represent the transmission loss factors at the end-face M1 and M2. R_1 and R_2 are the reflectivity at the end-face M1 and M2, respectively. The reference interference spectrum and other interference spectrums were subtracted respectively, and the absolute spectrum differentials were integrated along the interference spectrum. I_s is the reference intensity of interference spectrum, which is obtained by CL3 adaptive multi-wavelets (CL3-AMW) method. CL3 multi-wavelet has the characteristics of orthogonality, symmetry, second-order vanishing moment and tight support, and its support interval is [0,2]. The low-pass and high-pass filter coefficients of CL3 multi-wavelet are [31],

$$H_0 = 1/\sqrt{2}\begin{bmatrix} 1/2 & -1/2 \\ \sqrt{7}/4 & -\sqrt{7}/4 \end{bmatrix} \qquad (11)$$

$$H_1 = 1/\sqrt{2}\begin{bmatrix} 1 & 0 \\ 0 & 1/2 \end{bmatrix} \qquad (12)$$

$$H_2 = 1/\sqrt{2}\begin{bmatrix} 1/2 & 1/2 \\ -\sqrt{7}/4 & -\sqrt{7}/4 \end{bmatrix} \qquad (13)$$

$$G_0 = 1/\sqrt{2}\begin{bmatrix} 1/2 & -1/2 \\ -1/4 & 1/4 \end{bmatrix} \qquad (14)$$

$$G_1 = 1/\sqrt{2}\begin{bmatrix} -1 & 0 \\ 0 & \sqrt{7}/2 \end{bmatrix} \qquad (15)$$

$$G_3 = 1/\sqrt{2}\begin{bmatrix} 1/2 & 1/2 \\ 1/4 & 1/4 \end{bmatrix} \qquad (16)$$

The increase of basis function of multi-wavelet transform enhances higher degree of freedom in the construction process. According to the principle of biorthogonal multi-wavelet singular two-scale similarity transform (TSST), variable parameters can be added to the multi-wavelet construction process to obtain CL3-AMW.

The biorthogonal multi-wavelet singular TSST is [32],

$$H_{new}(\omega) = \frac{1}{2}M(2\omega)H(\omega)M^{-1}(\omega)$$
$$G_{new}(\omega) = G(\omega)M^{-1}(\omega) \qquad (17)$$

The corresponding inverse two-scale similarity transform (ITSST) is,

$$\breve{H}_{new}(\omega) = 2M^{-*}(2\omega)\breve{H}(\omega)M^*(\omega)$$
$$\breve{G}_{new}(\omega) = \breve{G}(\omega)M^*(\omega) \tag{18}$$

$M(\omega)$ is the TSST matrix. CL3-multi-wavelets can be obtained by performing two biorthogonal multi-wavelets singular TSSTs.

Two TSST matrices are,

$$M_1(\omega) = \begin{bmatrix} a(1+e^{-i\omega}) & -2\sqrt{2}a \\ b(1-e^{-i\omega}) & 0 \end{bmatrix} \tag{19}$$

$$M_2(\omega) = \begin{bmatrix} c & 0 \\ d(1+e^{-i\omega}) & f(1-e^{-i\omega}) \end{bmatrix} \tag{20}$$

Here, a, b, c, d are adaptive coefficients.

Firstly, $M_1(\omega)$ is brought into above formulas to obtain a new biorthogonal multi-wavelet. Then, $H(\omega)$ and $G(\omega)$ in Formula (17) are replaced by the obtained $H_{new}(\omega)$ and $G_{new}(\omega)$. $\breve{H}_{new}(\omega)$ and $\breve{G}_{new}(\omega)$ replace $\breve{H}(\omega)$ and $\breve{G}(\omega)$ in formula (18). The two-scale sign matrix $H_{final}(\omega)$, $G_{final}(\omega)$, $\breve{H}_{final}(\omega)$, $\breve{G}_{final}(\omega)$ of CL3-AMW can be obtained by taking $M_2(\omega)$ into formula (19) (20) and performing the second singular TSST. The twice singular TSST matrix contains variable parameters, which enables the CL3-AMW to adaptively change the basis function to achieve the best match between the multi-wavelet basis function and the pure water refractive index interference spectrum. I_s can be well obtained and subtracted from the other I_λ.

The total absolute differential power is,

$$I_\lambda - I_S = \frac{dI(\lambda)}{dRI}\delta RI \tag{21}$$

I_λ represents the light intensity of different refractive indices at the corresponding wavelength, and RI is the different refractive index corresponding to the wavelength. The integrated light intensity value is expressed by formula (22).

$$I_I = \sum_{\lambda_0}^{\lambda_n} |I_\lambda - I_S| \frac{\Delta\lambda}{RBW} \tag{22}$$

I_I is the integral light power. λ_0 is starting wavelength, λ_n is the cut-off wavelength, $\Delta\lambda$ is the wavelength step-size, RBW is the demodulator wavelength resolution.

Therefore, the level of I_λ approaching to I_s can be analyzed according to the improved SDI method, and the demodulation of refractive index can be realized.

3. Fabrication of micro-cavity

The femtosecond laser processing system is shown in Fig. 6. The laser is Libra-HE femtosecond pulsed laser. And it is equipped with a three-dimensional mobile platform. The main laser parameters are as follows: center wavelength is 800 nm, pulse width is $T_P = 100$ fs, repetition frequency is $f = 4.5$ kHz, maximum single pulse energy is E = 4.5 mJ. The attenuator and 1/2 wave-plate and polarizing beam splitter (PBS) are adopted to attenuate laser energy. The focusing lens is 20X with a NA=0.4.
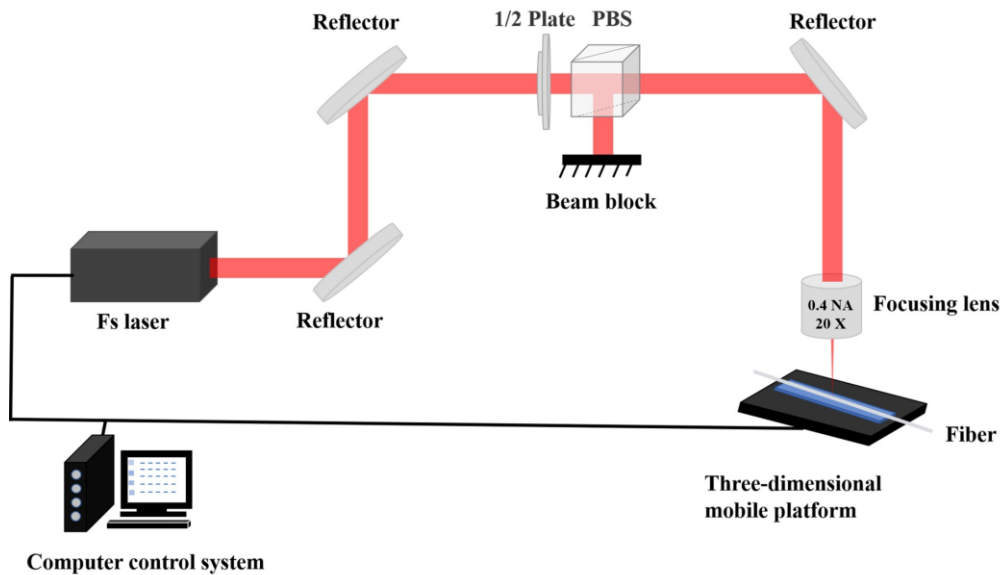

Fig. 6. Femtosecond laser processing system

When the femtosecond laser processes, laser beam passes through the focusing lens to form a focus spot, the diameter of focus spot is about D=2 µm. The etching path of light spot is shown in Fig. 7, and D_1 is the overlap distance of front and rear focus spots. D_2 is the distance between two adjacent etching lines.
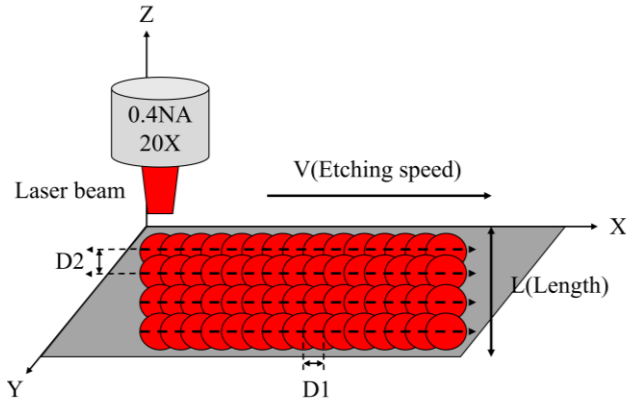

Fig. 7. Focus spot etching path and speed

The microscopic images of etched optical fiber are shown in Fig. 8, which are etched with different optical pulse energy and etching speeds. Fig. 8(a) illustrates the optical fiber surface with different etching speeds at a single pulse energy of 2 µJ. When the etching speed varies in the range of (0.1 mm/s ~ 0.9 mm/s), the micro-cavity edge is seriously chipping. When the etching speed is (1 mm/s ~ 2 mm/s), the chipping is reduced. However, while the etching speed is more than 2 mm/s, the overlap rate is zero, and the formed ablation on the optical fiber is not a continuous line but a dashed line. Fig. 8(b) demonstrates the optical fiber surface with different single pulse energy at the same etching speeds of 1.6 mm/s. When the single pulse energy is in the range of (1 µJ ~ 2 µJ), the micro-cavity chipping is less. As the single pulse energy continues to increase and exceeds 2 µJ, the micro-cavity chipping becomes more serious.
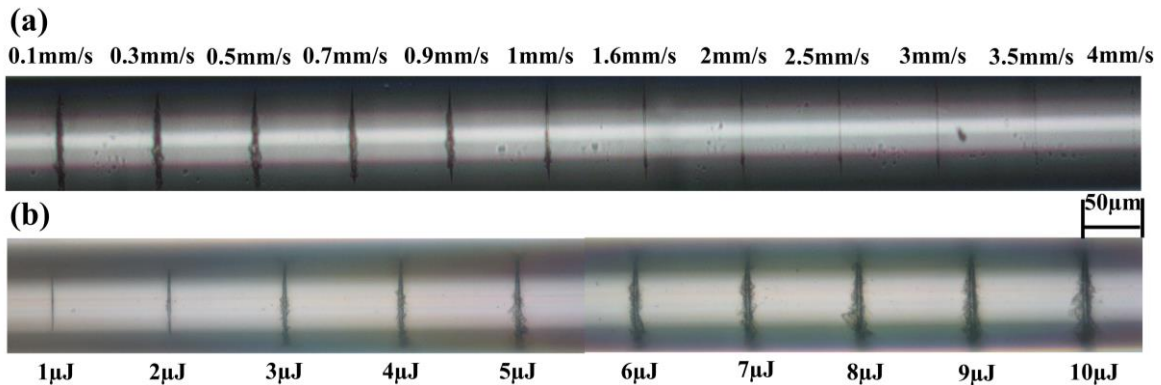

Fig. 8. Etching results with different processing parameter

When the etching speed is constant, larger is single pulse energy, larger is etching width. While the single pulse energy is constant, slower is etching speed, larger is etching width. When the single pulse energy and etching speed are (1 µJ, 1.6 mm/s) and (2 µJ, 1.6 mm/s), the etching lengths are 1.52 µm and 1.72 µm in Fig. 9(a). Similarly, while the single pulse energy and etching speed are (1 µJ, 1.6 mm/s) and (2 µJ, 1.6 mm/s), the etching depth are 4.15 µm and 5.80 µm in Fig. 9(b), respectively. Since the single etching depth is larger, the etching time is less, then, the etching efficiency is higher. So, the single pulse energy and etching speed are (2 µJ, 1.6 mm/s) for optimal processing parameters.
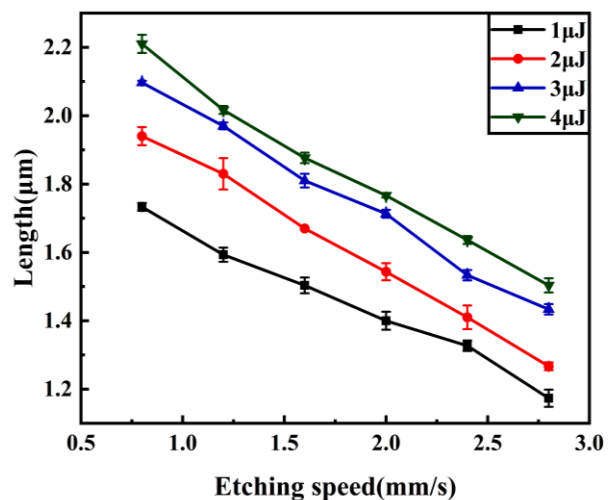

Fig. 9. Lengths with different processing parameters
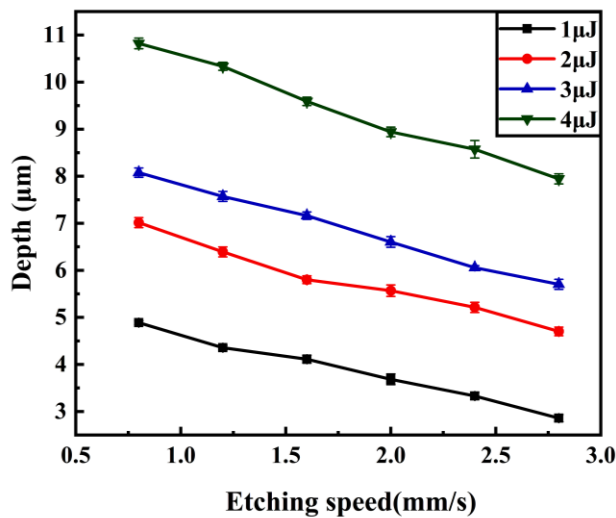(color online)

Fig. 10. Depths with different processing parameters (color online)

The laser single pulse energy is adjusted to 2 μJ, and the etching speed is adjusted to 1.6 mm/s. 27 etching lines are ablated along y direction, and the spacing between adjacent etching lines is D_2=0.86 μm along x direction, so, length L is obtained. Similarly, the etching is extended to the -z direction, with a step-size of 5.8 μm for each etching depth, and the vertical etching is performed for 13 times to obtain the etching depth. In order to get an optical fiber micro-cavity, 351 etching cycles are executed. Then, the optical fiber micro-cavity is immersed into 5% hydrofluoric acid solution for 5 minutes to remove residual impurities in the micro-cavity. Then, the hydrofluoric acid solution is cleaned by ultrasonic cleaning. Finally, the optical fiber micro-cavity is blown dry by nitrogen in Fig. 11.
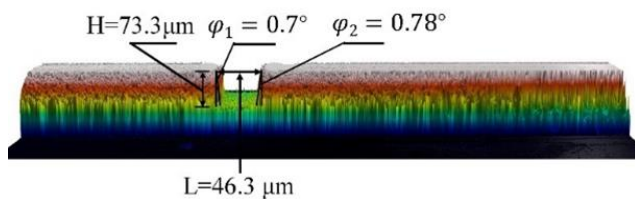

Fig. 11. Three-dimensional topography of optical fiber micro-cavity (color online)

The obtained length, depth, and end-face inclination of optical fiber micro-cavity are L=46.3 μm, H=73.3 μm, and φ_1=0.7°, φ_2=0.78°, respectively. The actual results of processed optical fiber micro-cavity meet the design specifications.

4. Results and discussion

4.1. Sensing experiment

The optical fiber refractive index sensing system of the Fabry-Perot micro-cavity is shown in Fig. 12. In order to obtain the sucrose refractive index sensing characteristics of optical fiber Fabry-Perot micro-cavity, different concentrations of sucrose solutions are prepared, and the sucrose refractive index of solutions is measured by an Abbe refractometer in the range of 1.342~1.372. Solutions of sucrose with different refractive indices were placed into separate beakers. The optical fiber Fabry-Perot micro-cavity was submerged into the beaker. The changes of interference spectrum were recorded by the demodulator. Subsequently, fiber optic Fabry-Perot micro-cavity was taken out from the solution and completely cleaned with distilled water. The corresponding relationships between the refractive index and interference spectrum of sucrose solution are obtained at 27 °C in Fig. 13. As the concentration of sucrose solution increases, the refractive index of sucrose solution is also increasing. Simultaneously, the interference spectrum shifts towards longer wavelengths, and the normalized maximum interference stripe contrast varies with the refractive index.
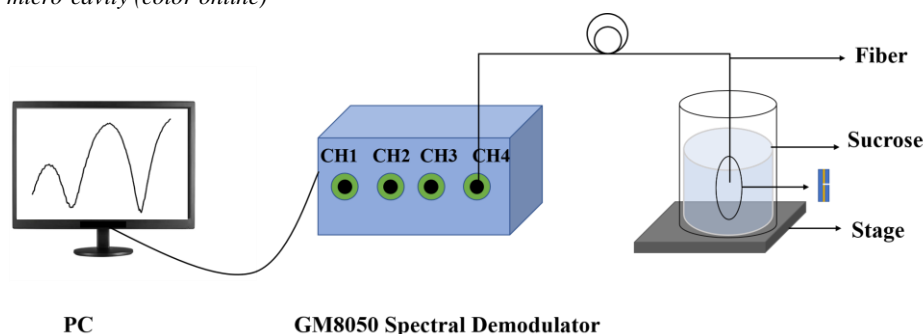

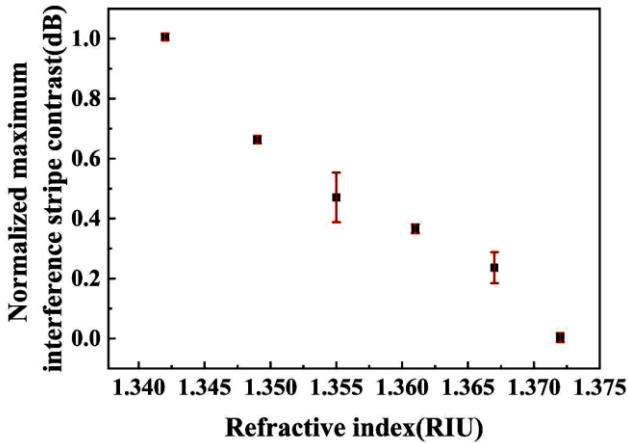*Fig. 12. Optical fiber* refractive index *sensing system*

Fig. 13. Relationship between normalized maximum interference stripe contrast and refractive index

After statistical calculation of 20 experiments, the relationship between normalized maximum interference stripe contrast and refractive index is in Fig. 14. The normalized maximum interference stripe contrast decreases monotonically with the increase of refractive index in the range of 1.342~1.372 (Refractive index unit, RIU). The sensor has good linearity and repeatability, and the correlation coefficient of linear regression is about 98.7% with a sensitivity of -30.69 dB/RIU.
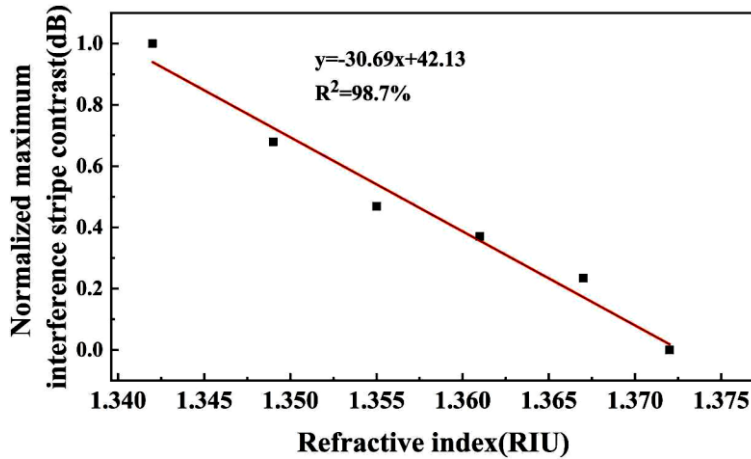

Fig. 14. Sensitivity and linearity by original SDI method

4.2. Optimized results

4.2.1. Improved data fusion algorithm

In the demodulation, the first step is to preprocess the collected data for eliminating the gross error. The Grubbs criterion is as follows: Assuming that the variables $x_{j1}, x_{j2}, \ldots, x_{jn}$ are measured, the mean value $\overline{x}_{j1}$ and the standard deviation σ_j are calculated by formula (23) and (24) [33].

$$\overline{x}_{j1} = \frac{1}{n} \times \sum_{i=1}^{n} x_{ij}, i = 1, 2, \cdots, n \tag{23}$$

$$\sigma_j = \sqrt{\frac{1}{n} \sum_{i=1}^{n} \left(x_{ij} - \overline{x}_j\right)^2} \tag{24}$$

According to the results of formula (23) and (24), the Grubbs statistic T_{ij} is calculated by formula (25),

$$T_{ij} = \frac{\left\| x_{ji} - \overline{x}_j \right\|}{\sigma_j} \tag{25}$$

T(n,a) is defined as the critical value of Grubbs criterion, where n=20 is the number of measurements, a=0.01 is the significant level. If $T_{ij} > T(n,a)$, data is an abnormal gross error, and data x_{ji} corresponding to T_{ij} should be eliminated. After removing the data, above judgment is repeated until all the data meet the Grubbs criterion. That is, there is no gross error. After preprocessing, the measured values of 20 tests are $X_1, X_2, X_3, \cdots, X_{20}$, which are independent of each other and are the unbiased estimation of X. The weighting

factors of each test result are $W_1, W_2, W_3, \cdots, W_{20}$ and $\hat{X}$ is the result of fusion algorithm in Fig. 15 [34].
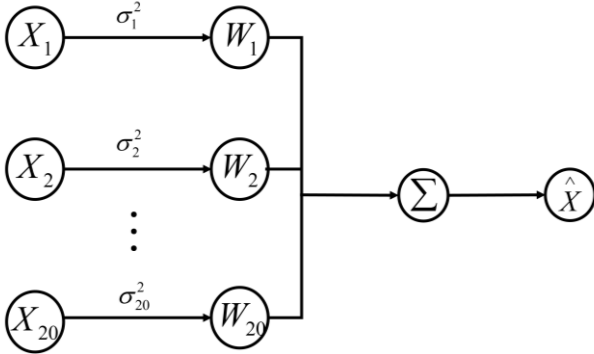

Fig. 15. Adaptive weighting algorithm

The fused $\hat{X}$ and weighting factor satisfy,

$$\hat{X} = \sum_{p=1}^{n} W_p X_p \qquad (26)$$

$$\sum_{p=1}^{n} W_p = 1 \qquad (27)$$

The total mean square error is,

$$\sigma^2 = E\left[(X - \hat{X}) \right]^2 \qquad (28)$$

Since $X_1, X_2, X_3, \cdots, X_{20}$ are independent of each other and are an unbiased estimate of X.

So,

$$E[(X - X_P)(X - X_q)] = 0, p \neq q, \\ p = 1, 2, 3, \cdots, 20; q = 1, 2, 3, \cdots, 20 \qquad (29)$$

It can be simplified as,

$$\sigma^2 = E\left[\sum_{p=1}^{n} W_P^2 (X - \hat{X})^2 \right] = \sum_{p=1}^{n} W_p^2 \sigma_p^2 \qquad (30)$$

σ^2 is a multivariate quadratic function of weighting factor W_p in formula (30). Each W_p is required, when σ^2 is minimum. By Lagrange multiplier method [35], the result can finally be got,

$$W_p = \frac{1}{\sigma_p^2 \sum_{p=1}^{n} \frac{1}{\sigma_p^2}}, p = 1, 2, 3, \cdots, n \qquad (31)$$

The minimum value of σ^2 is,

$$\sigma_{min}^2 = \sum_{p=1}^{n} \frac{1}{(\sum_{p=1}^{n} \frac{1}{\sigma_p^2})^2 \sigma_p^2} = \frac{1}{\sum_{p=1}^{n} \frac{1}{\sigma_p^2}} \qquad (32)$$

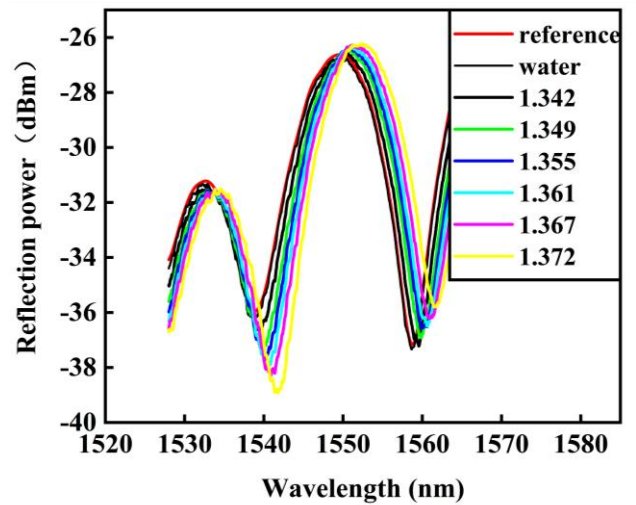Finally, the optimal $W_1, W_2, W_3, \cdots, W_{20}$ and $\hat{X}$ are obtained.

Fig. 16. Reflected interference spectrum by improved data fusion algorithm (color online)

After the gross errors are eliminated by improved data fusion algorithm, reference intensity of pure water interference spectrum processed by CL3 adaptive multi-wavelets (CL3-AMW) method in Fig. 16. The processed data is then demodulated utilizing the spectrum differential integration method. The light intensity of refractive index interference spectrum decreases with the increase of refractive index of sucrose solution. The normalized maximum stripe contrast was shown in Fig. 17. The refractive index sensitivity is -31.98 dB/RIU and linearity is $R^2 = 99.58\%$. Therefore, the improved spectral differential integral (ISDI) method is better than the results of original SDI method.
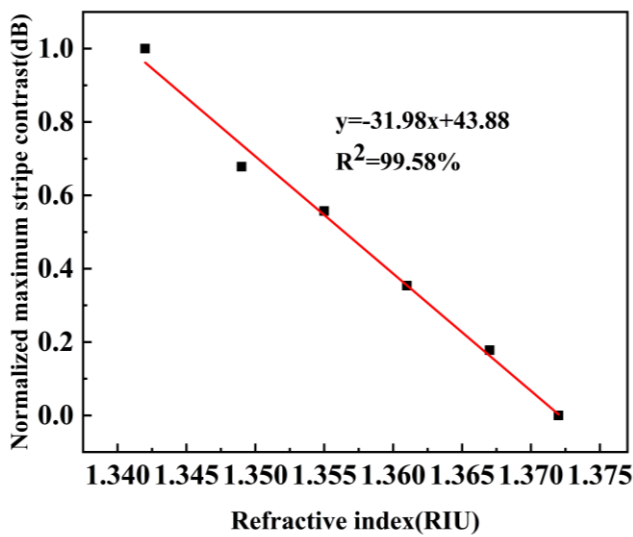
Fig. 17. Sensitivity and linearity by ISDI method

5. Conclusion

In this paper, an optical fiber Fabry-Perot microcavity sensor is designed and fabricated by femtosecond laser. The optimal etching parameters of fiber Fabry-Perot micro-cavity are obtained. Length of Fabry-Perot micro-cavity is $\in$ (45 μm ∼ 60 μm), height of Fabry-Perot micro-cavity is $\in$ (70 μm ∼ 75 μm), and inclined angle is $\varphi <$ 1.3°. The processed length, depth, and end-face inclination of optical fiber micro-cavity are L = 46.3 μm, H = 73.3 μm, and φ_1=0.7°, φ_2=0.78°, respectively. The proc essed optical fiber micro-cavity meets the design specifications. The sensor obtains that measuring sensitivity of sucrose refractive index is -30.69 dB/RIU and linearity is 98.7% by original SDI method. After using CL3-AMW method and improved data fusion algorithm, the sensitivity of sucrose refractive index attains -31.98 dB/RIU and linearity increases to 99.58%. The sensing performance of sucrose refractive index sensor is effectively enhanced. Overall, this research offers significant insights into the optimization design, fabrication of optical fiber Fabry-Perot micro-cavity sensor.

References

[1] M. Loyez, M. C. DeRosa, C. Caucheteur, R. Wattiez, Biosens. Bioelectron **196**, 113694 (2022).
[2] B. Glisic, Sensors-Basel **22**, 2397 (2022).
[3] M. D. Nadeem, S. K. Raghuwanshi, S. Kumar, IEEE Sens. J. **22**, 8090 (2022).
[4] J. Cai, Y. Liu, X. Shu, Sensors-Basel **23**, 542 (2023).
[5] Z. Qiu, R Mu, Y Zhang, Y. Li, Y. Teng, H. Li, Sensor Rev. **42**, 115 (2021).
[6] L. J. Li, X. Q. Wang, J. W. Li, Q. Jia, Y. Bo, Z. Liu, P. Zhang, Optik **260**, 169075 (2022).
[7] A. A. S. Falah, W. R. Wong, F. R. M. Adikan, Opt. Laser Technol **145**, 107474 (2022).
[8] W. Liu, T. Yang, Y. Shi, J. W. Yuming. D. Wu, Opt. Express **30**, 5618 (2022).
[9] R. Pan, W. Yang, L. Li, Y. Y. Qiang, Z. L. Jie, F. J. Ying, Y. Shuang, X. Y. Ling, IEEE Sens. J. **21**, 21577 (2021).
[10] K. Wang, Y. Mizuno, K. Kishizawa, Y. Toyoda, H. Lee, K. Ichige, W. Kurz, X. Dong, M. Jakobi, A. W. Koch, Jpn. J. Appl. Phys. **61**, 118001 (2022).
[11] S. Wang, J. Wang, W. Li, Y. Liu, J. Li, P. Jia, Micromachines-Basel **13**, 763 (2022).
[12] G. A. Lashari, F. Mumtaz, S. Ahmed, Opt. Fiber Technol. **74**, 103117 (2022).
[13] Q. Liu, C. Wang, W. Liu, Z. Rong, G. Hong, X. Wang, X. Qiao, Opt. Fiber Technol. **68**, 102794 (2022).
[14] D. Wang, Y. Wu, Y. Song, Y. Wang, L. Zhu, Opt. Fiber Technol **72**, 102989 (2022).
[15] X. Liu, Q. H. Wang, D. N. Wang, Optik **254**, 168642 (2022).
[16] M. Feng, S. Wang, S. Wang, L. L. Mao, Optik **193**, 162993 (2019).
[17] H. Z. Sun, C. Q. Jiang, J. R. Tang, W. Qi, Opt. Fiber Technol. **70**, 102890 (2022).
[18] X. Zhu, H. Chen, C. Jiang, X. Guo, H. Zhang, P. Wang, S. Sun, Opt. Fiber Technol. **71**, 102937 (2022).
[19] X. Zhang, X. Zhou, S. Wang, P. Tao, F. Ma, Q. Yu, W. Peng, Sensor. Actuat. A-Phys. **335**, 113375 (2022).
[20] Z. Zhang, J. W. Zhang, J. Y. Zhang, Optik **264**, 169409 (2022).
[21] N. Chen, L. Zhao, L. Chen, Liu, L. Yang, Opt. Fiber Technol. **164**, 109463 (2023).
[22] Z. Q. Lu, C. N. Liu, C. Li, J. Ren, L. Yang, Materials **16**, 3165 (2023).
[23] J. He, B. Xu, X. Xu, C. R. Liao, Y. P. Wang, Photonic Sens. **11**, 2 (2021).
[24] X. H. Liu, M. S. Jiang, Q. M. Sui, X. Y. Geng, F. R.

Song, Photonic Sens. **7**, 392 (2022).

[25] D. Wu, W. Huang, G. Y. Wang, J. Y. Fu, Y. Y. Chen, Opt. Commun. **313**, 70 (2019).

[26] X. H. Qi, L. Chen, B. Yan, Spectrosc. Spect. Anal. **41**, 1745 (2021).

[27] P. Zhou, C. R. Liao, Z. Y. Li, S. Liu, J. Light. Technol. **37**, 2835 (2019).

[28] S. N. Ma, Y. P. Xu, Y. X. Pang, X. Liu, Sensors **22**, 5722 (2022).

[29] G. Z. Wei, Q Jiang, Opt. Express **28**, 24586 (2020).

[30] S. Dalwinder, S. Birmohan, Pattern Recognit. **122**, 108307 (2022).

[31] J. de Villiers, D. Ranirina, Adv. Comput. Math. **45**, 7 (2019).

[32] G. Wang, Int. J. Wavelets Multi. **21**, 394 (2023).

[33] Y. Zhang, L. J. Gao, IEEE Access **7**, 2943916 (2019).

[34] N. Pan, Alex. Eng. J. **61**, 168 (2022).

[35] S. H. You, C. K. Ahn, S. Y. Zhao, Y. S. Shmaliy, IEEE T Ind. Electron. **69**, 55172 (2022).

_____

[*]Corresponding author: dun.liu@hbut.edu.cn